

Effect of motion path of downburst on wind-induced conductor swing in transmission line

Wenjuan Lou¹, Jiawei Wang¹, Yong Chen^{*1}, Zhongbin Lv² and Ming Lu²

¹*Institute of Structure Engineering, Zhejiang University, Hangzhou 310058, China*

²*Henan Electric Power Research Institute, Zhengzhou 450052, China*

(Received August 18, 2014, Revised June 21, 2016, Accepted June 23, 2016)

Abstract. In recent years, the frequency and duration of supply interruption in electric power transmission system due to flashover increase yearly in China. Flashover is usually associated with inadequate electric clearance and often takes place in extreme weathers, such as downbursts, typhoons and hurricanes. The present study focuses on the wind-induced oscillation of conductor during the process when a downburst is passing by or across a specified transmission line. Based on a revised analytical model recently developed for stationary downburst, transient three-dimensional wind fields of moving downbursts are successfully simulated. In the simulations, the downbursts travel along various motion paths according to the certain initial locations and directions of motion assumed in advance. Then, an eight-span section, extracted from a practical 500 kV ultra-high-voltage transmission line, is chosen. After performing a non-linear transient analysis, the transient displacements of the conductors could be obtained. Also, an extensive study on suspension insulator strings' rotation angles is conducted, and the electric clearances at different strings could be compared directly. The results show that both the variation trends of the transient responses and the corresponding peak values vary seriously with the motion paths of downburst. Accordingly, the location of the specified string, which is in the most disadvantageous situation along the studied line section, is picked out. And a representative motion path is concluded for reference in the calculation of each string's oscillation for the precaution of wind-induced flashover under downburst.

Keywords: multi-span conductor; flashover; moving downburst; motion path; wind-induced oscillation

1. Introduction

In the past decades, the ultra-high-voltage (UHV) and extra-high-voltage (EHV) transmission lines develop rapidly in China on account of their less land occupation and higher economic benefit. The subsequently farther electricity transmission distance will lead to a greater risk of encountering the severe weathers and complicated terrains. Recently, the frequency of the forced outage due to the wind-induced flashover, which is mostly associated with the insufficient air gap between the conductors and tower, increases markedly accounting for a poor operational reliability of the power supply system (Sun 2003). A recent statistical result has revealed that during 2005~2011, there were more than 751 wind-induced trips that took place in the transmission lines, whose electric levels are higher than 110kV, and triggered at least 376 outages in China (Lu 2014).

*Corresponding author, Associate Professor, E-mail: cecheny@zju.edu.cn

However, previous studies usually focused on the selections of the transmission line's wind load calculation methods and optimizations of the calculation parameters in the design code, e.g., reference wind velocity, span reduction factor, wind load adjustment factor and so forth (Wang *et al.* 2008, Jia *et al.* 2012, Long *et al.* 2006, Yan *et al.* 2010, Liu *et al.* 2009). Seldom studies took the extreme weathers, such as downbursts and tornadoes, into consideration. Nevertheless, some weather reports and field surveys of the accident areas (Hu 2004) had revealed that downbursts are extremely likely to be the cause of some flashovers.

Downburst, a downdraft which is often accompanied with thunderstorms and rainfalls, will produce a fairly high wind speed in several minutes near the ground. It has been proved to be a major cause of many transmission tower failures around the world (Savory *et al.* 2001, Hawes and Dempsey 1993, McCarthy and Melsness 1996, Dempsey and White 1996). Thereby, many probabilistic models for the design of transmission tower were proposed (Oliver *et al.* 2000, Li 2000), as well as many further studies of the transmission towers' behaviors during thunderstorm downbursts (Savory *et al.* 2001, Kanak *et al.* 2007, Shehata and EI Damatty 2007, Shehata and EI Damatty 2008). By using the finite element analysis (FEA) and optimization technology, the tower's critical members that are likely to fail during the downburst, and the corresponding configuration of the downburst were surveyed (Shehata *et al.* 2005, Shehata *et al.* 2008). In recent years, the bearing capacity (EI Damatty and Aboshosha 2012, Mara and Hong 2013) and response (Lin *et al.* 2012) of the tower, as well as the wind load distribution on the conductors (Aboshosha and EI Damatty 2013) under downbursts have gotten more attentions. Although many studies have taken into account the significant contribution of the conductors' wind loadings when considering the tower collapse, the wind-induced oscillation of conductor itself, which tends to trigger the flashover, is somewhat ignored.

As a typical wind-sensitive structure, the transmission line's load distribution along its length suffers a remarkable variation due to the time-varying distance between the studied conductors and storm center in the motion process of downburst. Thus, the motion path of a moving downburst is a crucial factor for the calculation of wind-induced oscillation of a specific multi-span transmission line, especially when the spans are different. Accordingly, this study generates the temporal wind field of a specified transmission line section, which is extracted from a practical 500kV UHV transmission line, under various moving downbursts with different motion paths primarily. Then in association with the precise finite element model, the relevant cases are numerically surveyed to get a comprehensive understanding of the effect of the motion path on the transient responses of the conductors. Eventually, a representative motion path is picked out so as to simplify the design work referring to the precaution of downburst-induced flashover. It is worth noting that, the present paper mainly focuses on the rotation angles of the suspension insulator strings (SISs), which could reflect the discrepancy of different SISs' risk of flashover more directly.

2. FEA Modelling of multi-span conductor

It is stated that the catenary is adopted to describe the initial shape of a conductor span under its own weight. Suppose that the sag length of a conductor span is f , the span length is L . If $f/L < 0.1$, the initial shape of a conductor under its own weight could be approximately regarded as a parabola (Sun 2010)

$$g(x_h) = \frac{4fx_h(L - x_h)}{L^2} + \frac{c}{L}x_h, \quad f = \frac{qL^2}{8T_H} \tag{1}$$

where $g(x_h)$ is the shape function of the conductor span, x_h is the horizontal distance from the head end of the conductor span, q is the conductor’s weight of per unit length, T_H is the horizontal tension of the conductor, and c is the discrepancy in elevation of two ends of the conductor span.

Thus, if parameters q , T_H and c are specified, the coordinate values of all points on a certain conductor span could be obtained through Eq. (1). Accordingly, an eight-span transmission line section, which incorporates conductors, 7 suspension insulator strings and 2 deadend strain insulator strings (DSISs), as briefly shown in Fig. 1, could be set up.

The relevant original parameters of conductors and insulator strings are illustrated in Table 1. The actual UHV transmission line employs 4-bundled sub-conductor, but Table 1 merely lists the parameters of one sub-conductor for reference. In the finite element model, the SISs could be simulated by using three-dimensional (3D) bar element, and the conductors could be modeled via 3D cable element. The DSISs are seen to be additional masses attached to relevant conductors in the original form finding.

The conductor’s initial tension is 25040 N. Most lengths of the cable elements are 10 m, and the total number of elements is about 300. Each SIS is hinged on its both sides. The wind loadings are imposed as nodal loads on both the insulator strings and conductors. The geometric nonlinearity is considered.

Before analyzing the multi-span conductor’s wind-induced oscillation, an imperative form finding should be conducted to import the additional masses aforementioned, which is related to the DSISs. Accordingly, the accurate initial stable shape of the studied transmission line section would be determined. Suppose that the height of i th node is z_i . Fig. 2 performs the determination process of the multi-span conductor’s initial stable shape, in which the wind load has not yet been imposed. It could be found that after the 1st form finding, the heights of some nodes on both of the terminal spans differ a lot from the original shape, which is earned by Eq. (1). Then a second form finding is taken, and the shape remains nearly unchanged.

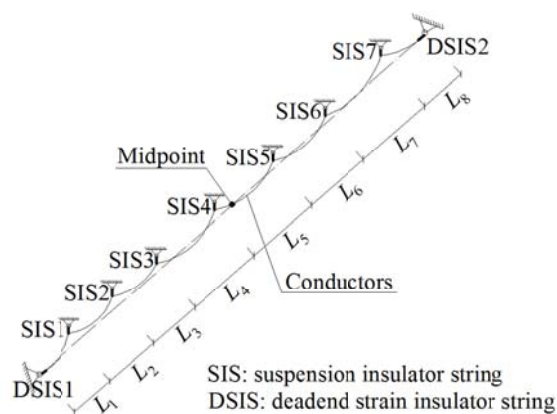


Fig. 1 Sketch of the studied multi-span transmission line section

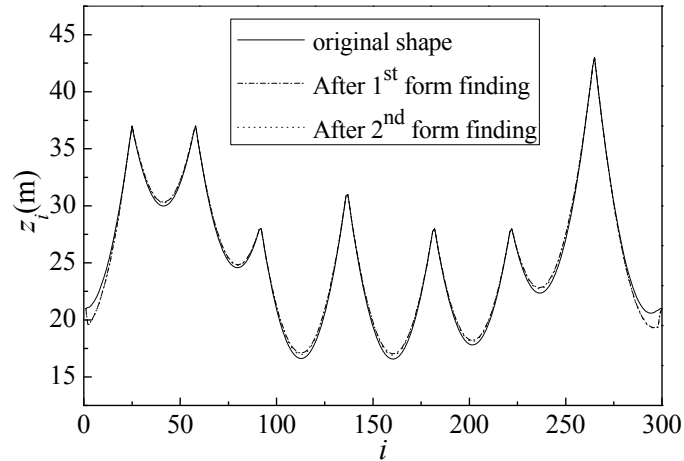


Fig. 2 Determination process of the multi-span conductor's initial stable shape

Table 1 Characteristic parameters of conductors and insulator strings

No. of the conductor span	Span length L_n (m)	Sag length f_n (m)	Insulator strings	Elevation of each string's hanging point (m)	Length L_{sN} (m)
$n=1$	228	3.431	DSIS1	21	7.64
2	326	7.014	SIS1	42	5
3	331	7.231	SIS2	42	5
4	441	12.840	SIS3	33	5
5	442	12.890	SIS4	36	5
6	393	10.193	SIS5	33	5
7	426	11.977	SIS6	33	5
8	331	7.231	SIS7	48	5
Total length L_t (m)	2918		DSIS2	21	7.64
Elasticity modulus E_C (N/m ²)	6.5E10		E_{SIS} (N/m ²)	3.0E10	
q_C (kg/m)	1.349		q_{SIS} (kg/m)	6.8	
External diameter D_C (m)	26.82E-03		D_{SIS} (m)	0.15	

3. Three-dimensional moving downburst simulation

For the stationary downburst, the wind field is axisymmetric with a high-pressure area at a specific distance away from the stagnation point (Chay and Letchford 2002). However, with regard to the long-span conductor, it seems that moving downburst is more harmful due to its larger damaging area. Meanwhile, its translational momentum will change the storm into a non-stationary event and lead to a strengthened wind field in the advancing side and a weakened one in the opposite side.

It has been documented that the vertical component of wind velocity would marginally affect the wind load of the transmission tower (EI Damatty and Aboshosha 2012). Meanwhile, the dynamic effect of the downburst load is negligible, because the period of oscillation of the load often far exceeds the towers' natural vibration periods (Shehata *et al.* 2005). However, in the calculation of the conductor's transient response, the dominated natural vibration periods of the conductor are usually longer than those of the tower's, and the vertical wind velocity will affect the wind directions, which might further influence the aerodynamic coefficients in the calculation of wind load. Thus, a three dimensional temporal wind field of the studied multi-span conductor under moving downburst, including mean and fluctuating components, is to be established to inspect the time-varying wind-induced oscillation of conductor accurately. In order to achieve the temporal wind field readily, the classical vector summation method (VSM) is used to obtain the low-frequency temporal mean component, whereas the deterministic–stochastic hybrid model (DSHM) is used to get the high-frequency fluctuating part.

Primarily, based upon the impinging jet model, a revised model proposed for the stationary downburst by Li *et al.* (2012) incorporating the nonlinear growth of boundary layer is chosen, which has been validated by the results of a detailed CFD (Computational Fluid Dynamics) simulation. In the analytical model, the radial and vertical mean wind velocity \bar{v}_i and \bar{w}_i of a certain point can be expressed as a function of its radial distance to the storm center, r_i , and height, z_i , respectively:

$$\begin{cases} \bar{v}_i(z_i, r_i) = v_{mm} v_{VS}(z_i) v_{RS}(r_i) \\ \bar{w}_i(z_i, r_i) = v_{mm} \mu_z w_{VS}(z_i) \mu_r w_{RS}(r_i) \end{cases} \quad (2)$$

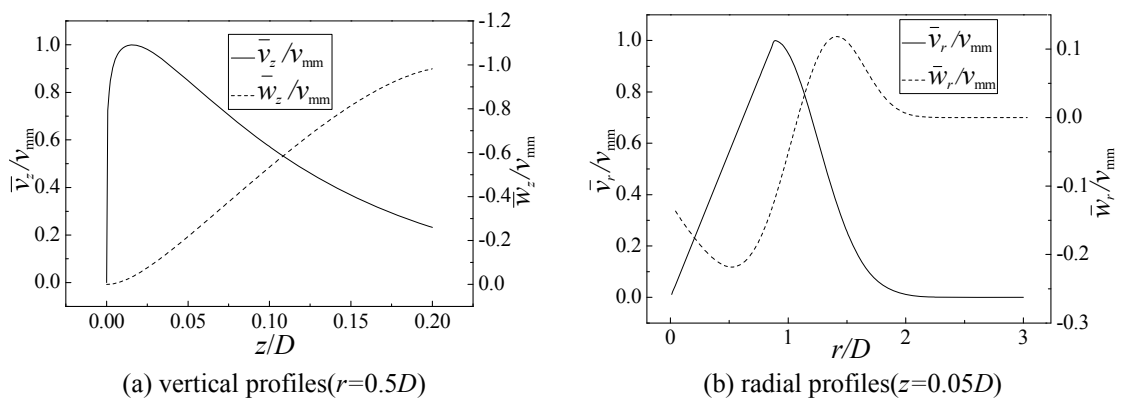


Fig. 3 Radial and vertical profiles of the wind velocities

where, v_{mm} is the maximum wind velocity in the entire stationary downburst, v_{VS} and w_{VS} are the vertical profile functions of the radial and vertical wind velocity respectively, while v_{RS} and w_{RS} are the radial profile functions, μ_r and μ_z are two normalizing factors. Let the jet diameter of downburst be 1000 m, then the normalized wind velocity profiles are depicted in Fig. 3.

In the moving downburst, r_i is a function of time t as a result of the constantly moving storm center. Let the jet diameter be D , the translation speed of downburst be V_m , and the simulation time length be t_0 . It is worth noting that the variation of V_m in the height range of conductors is not considered here and when assigning the value of t_0 , the duration time and damaging area of the storm should be taken into account. The calculation cases herein fall into two categories.

The first category refers to the cases that the downburst would pass by the transmission line, i.e. the motion paths are parallel to the transmission line, in the horizontal projection plane. A Cartesian coordinate system, whose original point is set at the starting of the entire transmission line section, is built in the projection plane, as shown in Fig. 4(a). Its y axis is along the direction of conductor. The time-varying distance between the i th node P_i and the storm center, $r_i(t)$, can be presented as follows:

$$r_i(t) = \sqrt{d^2 + (y_i + |y_0| - V_m \cdot t)^2} \tag{3}$$

where d is a critical variable as a representation of the horizontal distance between the motion path and conductors, x_0 and y_0 are the coordinates of the initial storm center, $x_0 = -d$, $y_0 = \frac{L_t - L_c}{2}$, L_t is the total length of the multi-span transmission line section, L_c is the calculation length of the motion path of downburst, $L_c = V_m t_0$, y_i is the y coordinate of the certain point P_i on the conductor.

The second category refers to the cases that the motion paths intersect with the transmission line in the horizontal projection plane. Then, the intersection point is set to be the original point and y axis is also along the conductor, as shown in Fig. 4(b). In similar fashion, we have

$$r_i(t) = \sqrt{\left(|x_0| - \frac{1}{2} V_m t \sin \alpha_m \right)^2 + \left(y_i + |y_0| - \frac{1}{2} V_m t \cos \alpha_m \right)^2} \tag{4}$$

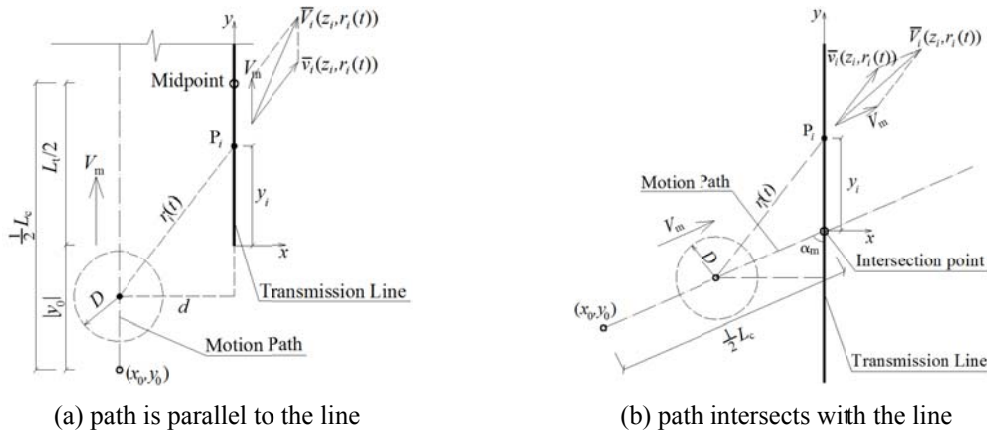


Fig. 4 Sketches of the VSM corresponding to different motion paths

where α_m is the angle between the motion path and transmission line, $x_0 = -\frac{1}{2}L_c \sin \alpha_m$,
 $y_0 = -\frac{1}{2}L_c \cos \alpha_m$.

By using VSM, the temporal mean radial wind velocity of each element node on the conductor, $\bar{V}_i(z_i, r_i(t))$, could be attained. Then both the radial and vertical fluctuating wind speed could be expressed as the product of an amplitude modulation function and a stationary Gaussian stochastic process (Chen and Letchford 2004, Pan *et al.* 2008)

$$\begin{cases} \tilde{v}_i(z_i, r_i(t)) = a_i(z_i, r_i(t)) \cdot \psi_i(z_i, t) \\ \tilde{w}_i(z_i, r_i(t)) = a_i(z_i, r_i(t)) \cdot \zeta_i(z_i, t) \end{cases} \quad (5)$$

Where $a_i(z_i, r_i(t)) = I(z_i) \cdot \bar{V}_i(z_i, r_i(t))$ (6)

and (Chen and Letchford 2005)

$$I(z_i) = 0.088 \times (10 / z_i)^{\frac{1}{6}} \quad (7)$$

In Eq. (5), $\psi_i(z_i, t)$ and $\zeta_i(z_i, t)$ can be obtained via DSHM, in which the normalized power spectrum density (PSD) models proposed by Kaimal et.al and Panofsky et.al respectively are used.

4. Aerodynamic coefficients' measurement tests

4.1 Equipment and test models

In order to obtain the accurate aerodynamic coefficients of the specific 4-bundled conductors aforementioned, the wind tunnel tests were conducted in ZD-1 boundary layer wind tunnel in Zhejiang University. The size of its test section is 4 m (width) × 3 m (height) × 18 m (length). The wind tunnel is supplied by a 1000 kW direct current motor, and the test wind speed ranges from 3 ~ 55 m/s. The high frequency force balance (HFFB), which is made by ME-SYSTEM Corporation, was used to measure the three component aerodynamic forces, including two forces and a moment. In the current test, the upper measuring limit of the HFFB was set to be 20 N for force and 4 N·m for moment respectively, and the sampling frequency was 500 Hz.

The truncated rigid model (TRM), which was used to simulate the sub-conductor, was made by wood and would be twined by some plastic bubble strips to take the sub-conductor's surface roughness into account, as shown in Fig. 5. Meanwhile, the TRM had a plexiglass base plate to provide a reliable fixation in the experiments. To introduce the mutual shielding effect between the sub-conductors, all the 4 sub-conductors were built in the tests. Moreover, two clapboards were set up to generate a two-dimensional (2D) homogeneous turbulence, as shown in Fig. 6.

4.2 Equivalent aerodynamic coefficients

For the future investigation of the single sub-conductor's wind-induced response and usage quantity saving of the HFFB, only one sub-conductor's three component aerodynamic forces were

sampled, which were denoted by R_{S1} , R_{S2} and M_S . As the forces of the fixed sub-conductor were measured under all the wind attack angles from $0 \sim 345^\circ$ with an interval of 15° , the remaining sub-conductors' aerodynamic forces under a specific wind attack angle can be obtained through the symmetry principle as follows

$$\begin{cases} R_{A1}(\gamma_t) = -R_{S1}(\gamma_t + 90^\circ), R_{A2}(\gamma_t) = -R_{S2}(\gamma_t + 90^\circ) \\ R_{B1}(\gamma_t) = -R_{S2}(\gamma_t + 180^\circ), R_{B2}(\gamma_t) = R_{S1}(\gamma_t + 180^\circ) \\ R_{C1}(\gamma_t) = R_{S2}(\gamma_t + 270^\circ), R_{C2}(\gamma_t) = -R_{S1}(\gamma_t + 270^\circ) \end{cases} \quad (8)$$

where A, B and C are the serial number of the un-sampled sub-conductors, γ_t is the angle between R_{S1} and incident flow, $0 \leq \gamma_t \leq 90^\circ$, as depicted in Fig. 7.

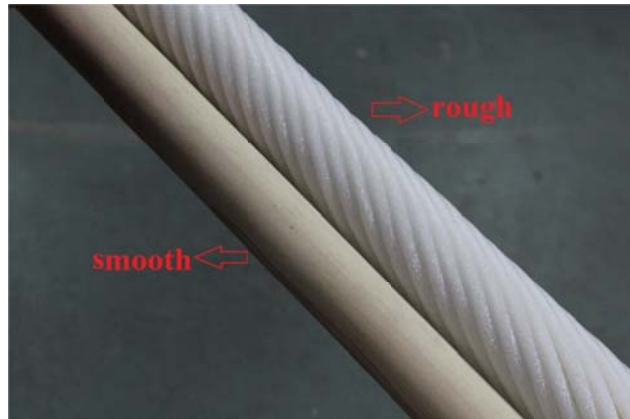


Fig. 5 Truncated rigid model

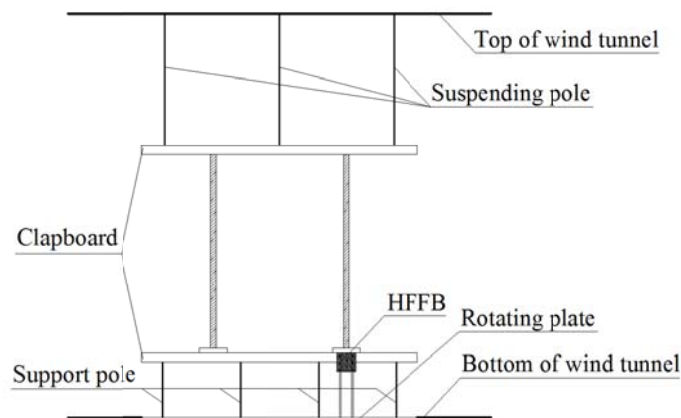


Fig. 6 Experiment setup

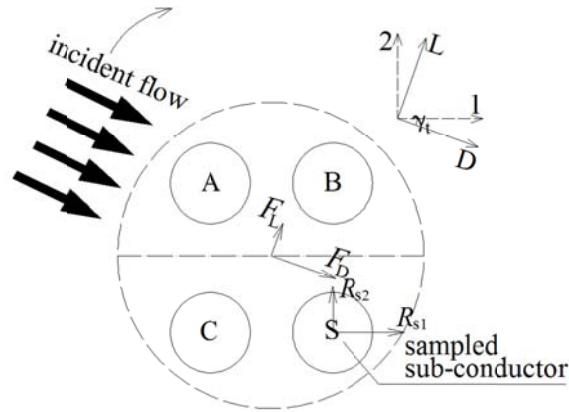


Fig. 7 Sketch for the acquisition of the unsampled sub-conductors' forces

In the current study, the 4-bundled conductor is regarded as a whole, so the whole equivalent aerodynamic coefficients, including the drag coefficient (C_D) and lift coefficient (C_L), are mainly concerned, which could be calculated by

$$C_D = \frac{\bar{F}_D}{\frac{1}{2} \rho_a U_i^2 A_w}, \quad C_L = \frac{\bar{F}_L}{\frac{1}{2} \rho_a U_i^2 A_w} \quad (9)$$

where, ρ_a is the density of air, U_i is the wind speed of the incident flow, A_w is the windward area of the 4-bundled conductor, \bar{F}_D and \bar{F}_L are the mean values of F_D and F_L in the time domain respectively, $F_D = R_{t1} \cos \gamma_t - R_{t2} \sin \gamma_t$, $F_L = R_{t1} \sin \gamma_t + R_{t2} \cos \gamma_t$, $R_{t1} = R_{S1} + R_{A1} + R_{B1} + R_{C1}$, $R_{t2} = R_{S2} + R_{A2} + R_{B2} + R_{C2}$.

4.3 Effect of Reynolds number

For the flow around a circular cylinder, Achenbach and Heinecke (1981) had revealed that there are six regimes based on visual observation. According to the summary raised by Raghavan and Bernitsas (2011), the characteristic regimes and the corresponding ranges of Reynolds number (Re) are shown in Fig. 8.

Actually, for the sub-conductor, the Reynolds number often lies in the range approximately from 10^4 to 10^5 , which corresponds to the subcritical regime. In this Re range, it had been revealed that for the circular cylinder with a smooth surface, the drag coefficient C_D almost remains unchanged, but it might not make sense if the surface roughness is taken into consideration (Achenbach and Heinecke 1981). Thus, an investigation of the effect of the Reynolds number on the rough sub-conductor's C_D should be conducted.

In this part, a 2D uniform flow was adopted in order to obtain a largest possible variation range of the Reynolds number of the flow around the sub-conductor, which could be calculated by

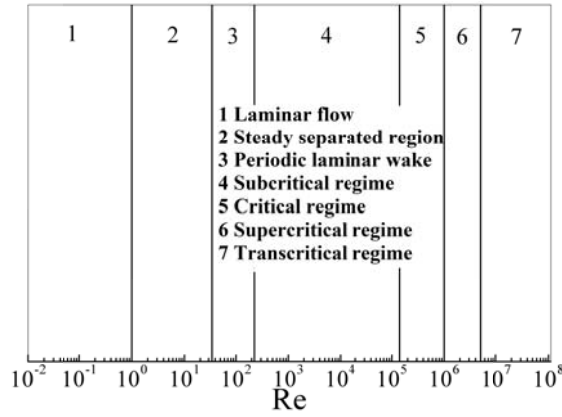


Fig. 8 Characteristic regimes of the flow around a circular cylinder in different Re ranges

$$Re = \frac{U_i d_c}{\nu_a} \tag{10}$$

where, d_c is the diameter of sub-conductor’s twined TRM, $d_c=39.5$ mm, ν_a is the kinematic viscosity of air corresponding to the actual temperature and pressure in the wind tunnel, $\nu_a = 1.62 \text{ m}^2/\text{s}$, U_i is the wind speed of incident flow, which ranges from 5 ~ 30 m/s with an interval of 2.5 m/s.

In the tests, $\gamma_t = 0^\circ$, and the variation of C_D under different Re is shown in Fig. 9. It could be found that in the Re range here, the curve of C_D declines at first and then nearly remains flat till the end. Thus when considering the values of C_D in the 2D homogeneous turbulent flow in the following study, the wind speed of incident flow is set to be 15 m/s, and the corresponding C_D under different γ_t is performed in the paper’s later part.

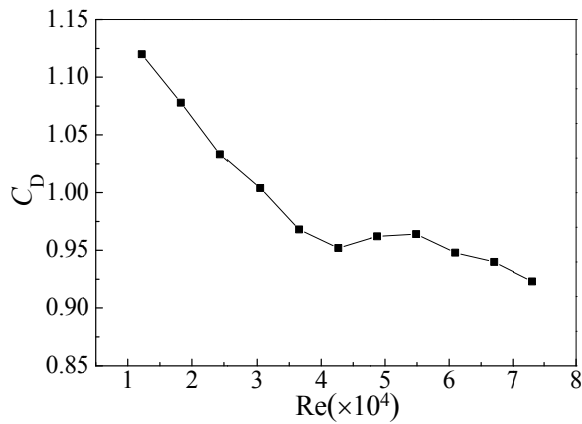


Fig. 9 Variation of C_D under different Re

5. Downburst wind load calculation

For the calculation of out-of-plane oscillation of the long-span conductor, the wind load, which is in the direction perpendicular to the transmission line (i.e., the x direction in Fig. 4), plays a dominant role. According to the quasi-steady assumption, the vertical and horizontal wind loadings on its node of the conductor could be computed by

$$\begin{cases} F_{zi} = \frac{1}{2} \rho_a C_{zi} A_i V_{ir}(z_i, r_i(t))^2 \\ F_{xi} = \frac{1}{2} \rho_a C_{xi} A_i V_{ir}(z_i, r_i(t))^2 \end{cases} \quad (11)$$

where, ρ_a is the density of air, A_i is the windward area of the i th node, C_{zi} and C_{xi} are the aerodynamic coefficients for the i th node in directions of z and x coordinates respectively, and could be calculated by

$$\begin{cases} C_z = C_D(\gamma) \sin \gamma_w + C_L(\gamma) \cos \gamma_w \\ C_x = C_D(\gamma) \cos \gamma_w + C_L(\gamma) \sin \gamma_w \end{cases}, \quad \gamma = \gamma_w - \gamma_c, \quad \gamma_w = \arctan \left[\frac{W_i(z_i, r_i(t)) - w_{ir}(t)}{U_{ix}(z_i, r_i(t)) - v_{ir}(t)} \right] \quad (12)$$

where C_D and C_L are equivalent drag and lift coefficients respectively, which could be obtained through Eq. (9), γ is the wind attack angle, γ_c is the deflection angle of sub-conductor, as shown in Fig. 10.

In Eq. (11), $V_{ir}(z_i, r_i(t))$ is instantaneous relative wind speed, thus the transient motion state of the conductor itself could be taken into consideration,

$$V_{ir}(z_i, r_i(t)) = \sqrt{[V_{ix}(z_i, r_i(t)) - u_{ir}(t)]^2 + [W_i(z_i, r_i(t)) - w_{ir}(t)]^2} \quad (13)$$

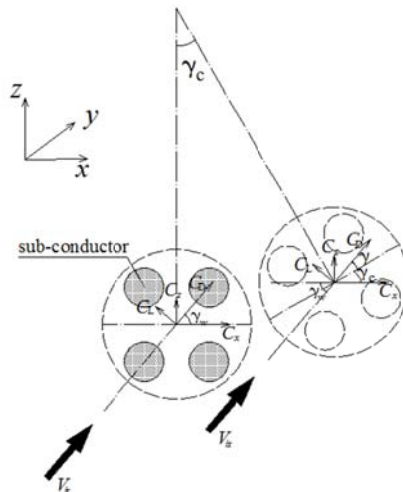


Fig. 10 Sketch for the calculations of C_z and C_x

where $u_{it}(t)$ and $w_{it}(t)$ are the velocities in x and z directions of the i th node of the conductor undergoing vibration, and $V_{ix}(z_i, r_i(t))$ could be computed by

$$V_{ix}(z_i, r_i(t)) = V_i(z_i, r_i(t)) \sin \beta_u \quad (14)$$

where β_u is the angle between $V_i(z_i, r_i(t))$ and transmission line.

In Eqs. (13) and (14), $V_i(z_i, r_i(t))$ and $W_i(z_i, r_i(t))$ are the total velocities of the horizontal and vertical wind respectively, which could be obtained by

$$\begin{cases} V_i(z_i, r_i(t)) = \bar{V}_i(z_i, r_i(t)) + \tilde{v}_i(z_i, r_i(t)) \\ W_i(z_i, r_i(t)) = \bar{W}_i(z_i, r_i(t)) + \tilde{w}_i(z_i, r_i(t)) \end{cases} \quad (15)$$

6. Case study

In case studies, in order to make most of the entire transmission line section lie in the high wind speed area of the downburst in the height range, the jet diameter of the downburst, D , is set to be 1250 m. Based upon the value of wind velocity in the design process, let $v_{\text{mm}}=25$ m/s. The remaining calculation parameters $V_m=v_{\text{mm}}/3$, $t_0=1024$ s, C_D and C_L under different wind attack angles are listed in Table 2 (for simplicity's sake, only the values in the γ range from 0° to 45° are listed, and the remains could be obtained through the symmetry principle). In accordance with Table 2, it is found that C_L is relatively small in comparison with C_D . Moreover, in case of listed wind attack angles except 0° , C_D is about 1.0. Thus, in the following computing, the lift force is ignored and the value of C_D is set to be 1.0.

Various calculation cases corresponding to multiple motion paths, which fall into two categories aforementioned, are studied to gain a comprehensive understanding of the conductors' transient responses. For each case, a transient analysis is performed, whereby the time-histories of displacements of the nodes could be attained, namely $d_x(t)$, $d_y(t)$ and $d_z(t)$. Subsequently, the time-varying rotation angle of each SIS, $\theta(t)$, is calculated, which has an advantage in the comparison of the air gaps of SISs with different lengths. The rotation angle could be calculated by

$$\theta_N(t) = \arcsin \frac{d_{xN}(t)}{\sqrt{l_{sN}^2 - d_{yN}(t)^2}} \quad (16)$$

where the subscript N represents the sequential number of SIS, l_{sN} is the length of N th SIS.

Table 2 Measured C_D and C_L under various wind attack angles

$\gamma(^{\circ})$	0	9	18	27	36	45
C_D	0.934	0.990	1.012	1.010	1.009	0.982
C_L	0.022	0.011	0.004	-0.009	-0.011	-0.006

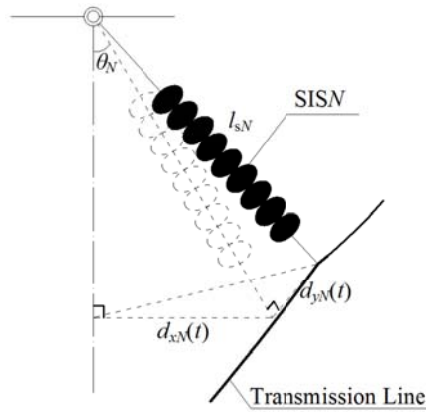


Fig. 11 Calculation method of the Nth SIS's rotation angle

In the calculations of $\theta(t)$ in the atmospheric boundary layer, $d_x(t)$ is a critical indicator to verify the electric clearance directly while $d_y(t)$ is often ignored because it is perpendicular to the swing plane and often believed to be negligible. However, due to the relatively small damaging area of the moving downburst, the wind load difference between the adjacent spans will be larger, which may increase the displacement of SIS in the y axis direction. Thus, as shown in Eq. (16), the equivalent length of SISN, i.e. the denominator, is adopted and the SIS is projected onto the plane that is perpendicular to the transmission line, as depicted in Fig. 11.

In the following discussions, 28 cases are included to introduce various relative positions between the transmission line and storms, covering nearly all typical situations. The effect of motion paths of downbursts will be mainly embodied through the differences of each SIS's maximum rotation angle θ_{Nmax} in the time domain in each case. Then, each SIS's peak rotation angle, θ_{Nmm} , which is widely used to check the electric clearance in the design process of transmission towers in China, is concluded from the total 28 cases and presented as well.

6.1 Motion path is parallel to the transmission line

In the case of that the motion path of downburst is parallel to the line, four situations are taken into account that is to say d is set to be $0.6D$, $0.8D$, $1.0D$ and $1.2D$ respectively, in terms of the damaging areas of the downbursts. Fig. 12, which could also represent the variations of responses in the remaining three cases, presents the time-varying displacements of SIS4 in the horizontal plane and the rotation angles of SIS1, SIS4 and SIS7 in the case of that $d=1.0D$. It is found that θ_N is approximately proportional to d_{xN} . In the motion process of the downburst from the starting of the motion path to the end, each SIS's θ_N only has a rapid increase in several minutes and approaches merely zero in the remain time. Meanwhile, the rotation angles of the SISs get different peaks successively. This indicates that in these cases the flashover of different SIS may not occur at the same time and the time intervals depend on the length of each span and the translation speed of downburst.

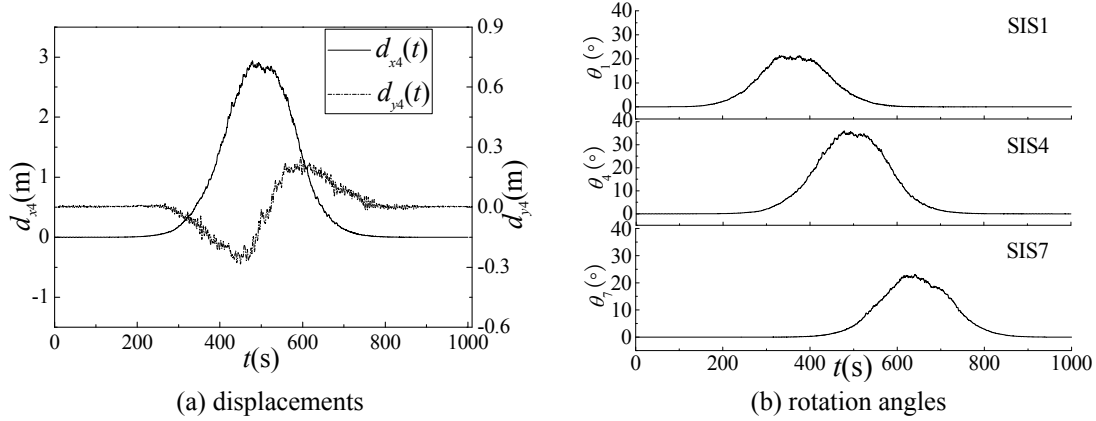


Fig. 12 Time-history curves of the responses in the first category

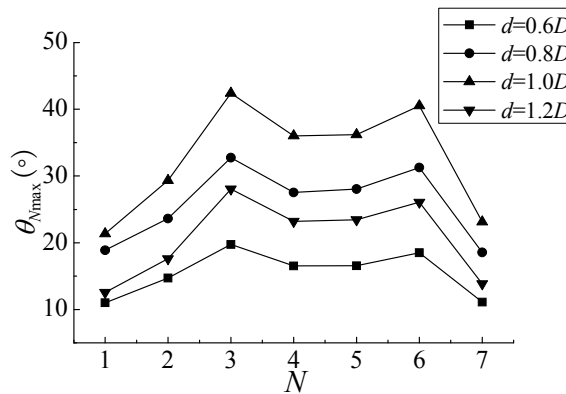


Fig. 13 θ_{Nmax} of each SIS in the 4 cases in the first category

Comparison of each SIS's maximum rotation angle θ_{Nmax} in each case is conducted and the results are summarized in Fig. 13. From the figure, a similar trend, that the extremums of the SISs' wind-induced oscillations along the entire line always occur at SIS3 and SIS6, can be found in all the 4 cases. Furthermore, it can be found that when $d=1.0D$, it seems to be the most disadvantageous for all SISs, which is mainly as a result of the distinct radial wind speed profile of the downburst, as shown in Fig. 3(b). Meanwhile, it should be noticed that when d takes a smaller value, V_{iy} increases while the concerned V_{ix} decreases, which will lead to a reduction of the concerned wind load in the direction perpendicular to the transmission line.

6.2 Motion path intersects with the transmission line

Various cases are considered likewise in which the intersection point locates at the position of SIS4, midpoint (lies between SIS4 and SIS5), SIS5, SIS6 and α_m varies from 15° to 90° with a

specified interval of 15° . Fig. 14 shows the time-history results of the displacements of SIS4, including $d_{x4}(t)$ and $d_{y4}(t)$, and the corresponding rotation angles of SIS1, SIS4, and SIS7 in the case of that the intersection point locates at the midpoint and $\alpha_m=90^\circ$. Obviously, $\theta(t)$ experiences a relatively large positive peak and a minor negative one in the motion process of downburst, which is different from that in the first category. This is mainly due to that when a downburst passes across the transmission line, the direction of the radial wind velocity reverses. And the discrepancy of the peak values is due to the translational momentum of the moving downburst, which will lead to an asymmetric pressure distribution in the surrounding area of storm center.

In addition, concluding from all the calculation results(including both categories), it can be found that despite the fact that a larger d_y may occur in the first category, d_y is still considerable compared to d_x in some cases especially when the lengths of considered adjacent spans differ a lot. Moreover, it is found that fluctuating component of wind speed has a slight contribution to the results, which may be due to the low turbulence intensity adopted or the introduction of conductor's motion state in the present study. Furthermore, compared to the results in the atmospheric boundary layer, the variations of the rotation angles here suffer a gentle change in the time domain, which can approximately be seen as a long period change. Yet this is disadvantageous to the flashover because its lengthened duration of crisis will decrease the success rates of automatic reclose.

The results of the whole transmission line section are processed in the way the same as employed for the cases in the first category, and depicted in Fig. 15. It can be found that, in many cases, the results of θ_{Nmax} exceed the values in the cases that belong to the first category, especially the cases in which α_m has a large value. It indeed means a higher risk of flashover. In the aspect of whether variation trend or value, a big difference is found if the motion path changes. From the results shown, an overall increasing trend of each SIS's θ_{Nmax} with the enhanced α_m in a specified range could be found. This is mainly due to the increase of V_{ix} . Furthermore, in the cases of that α_m is small, when the intersection point moves from the middle part of the transmission line to the endpoint, the overall trend of all the 7 SISs' θ_{Nmax} remains unchanged, and the extremum, whose value gradually increases with α_m , takes place at SIS2 or SIS3. In the cases of that α_m is relatively large, the location variations of the intersection point will strengthen the inhomogeneity of the wind pressure distribution along the line section, and the location of the extremum will move to be adjacent to where the intersection point lies.

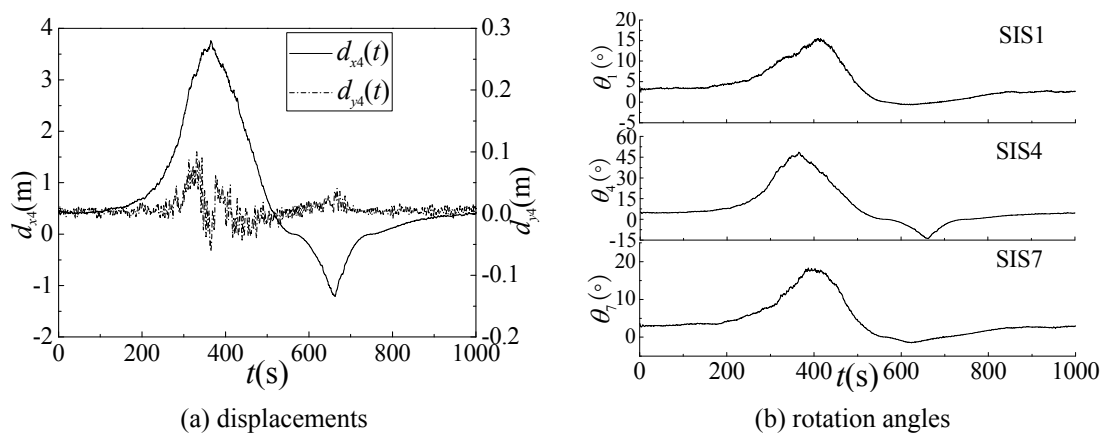


Fig. 14 Time-history curves of the responses in the second category

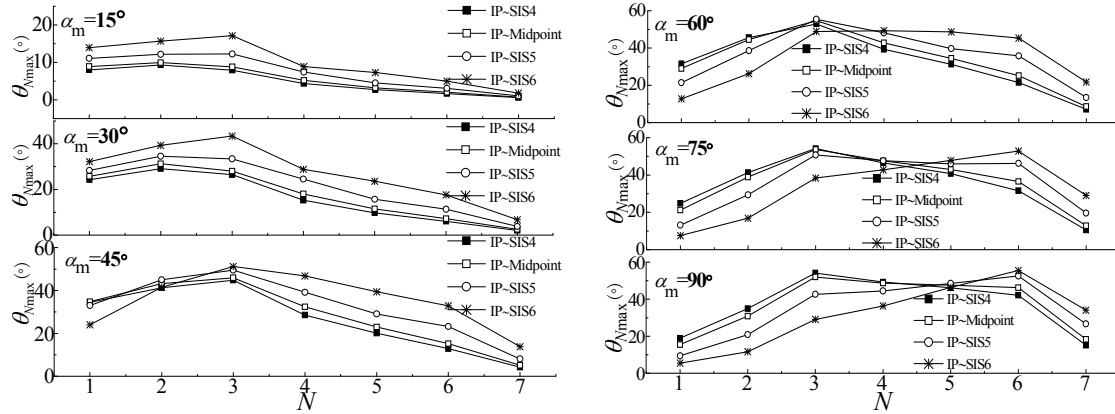


Fig. 15 θ_{Nmax} of SIS1 ~ 7 in all the 24 cases in the second category

A further statistical analysis has been applied to the data. The sequential number of SIS, which is found to be the most dangerous in each certain case, is listed in Table 3. Mostly, for the studied transmission line section, SIS3 seems to be in the most adverse situation rather than the SIS overlapped with the intersection point, which may be induced by the relatively large value of the jet diameter compared with each span length.

Meanwhile, concluding from the results of all the calculation cases, it is found that compared to the either SIS at the endpoints of the line section, the remaining SISs suffer a higher risk of flashover. Furthermore, mostly when the downburst moves directly through the SIS with a motion path perpendicular to the transmission line, it poses a greatest threat to the specific SIS. Actually, in the design process of a specific tower, the peak rotation angle of each SIS θ_{Nmm} is mainly concerned, rather than the corresponding motion paths. Thus, in order to simplify the design process, this specific motion path might be seen as a representative of the various calculation cases when considering a given SIS. With some additional calculations, the results of all SISs' representative cases are complemented, as listed in Table 4, as well as the final results of θ_{Nmm} considering all the calculation cases (including the representative cases). Obviously, some SISs' (e.g., SIS1, SIS4, SIS5) results of θ_{Nmm} exceed the results of θ_{Nmax} of their respective representative cases just a little bit. However, the results of the representative cases are still proved to reflect the results of all cases in an acceptable range.

Table 3 No. of the SIS which suffers the greatest risk of flashover in each motion path

$\alpha_m(^{\circ})$	Location of the intersection point			
	SIS4	Midpoint	SIS5	SIS6
15	2	2	3	3
30	2	2	2	3
45	3	3	3	3
60	3	3	3	4
75	3	3	3	6
90	3	3	6	6

Table 4 Comparison of $\theta_{N_{\min}}$ concluded from all cases with $\theta_{N_{\max}}$ in the representative cases

N	$\theta_{N_{\min}}$ (°)	Location of the intersection point	α_m (°)	$\theta_{N_{\max}}$ in the representative cases (°)
1	34.79	Midpoint	45	34.52
2	45.80	SIS2	90	45.80
3	55.58	SIS3	90	55.58
4	49.33	SIS6	60	49.22
5	48.72	SIS6	60	48.51
6	55.49	SIS6	90	55.49
7	35.93	SIS7	90	35.93

7. Conclusions

This paper investigates the effects of motion paths on the wind-induced conductor swing of the transmission line under moving downburst. The results show that:

- In the case of that the motion path is parallel to the transmission line, the temporal response of each SIS reaches its peak value successively, and the most adverse situation occurs when $d=1.0D$.
- In the case of that the downburst moves across the conductors, there is a relatively large positive peak and a minor negative peak in the time-history curve of each SIS's rotation angle. The location of critical SIS that suffers a greatest risk of flashover along the entire line section, and the corresponding maximum rotation angle directly depend on the motion path of downburst, and are also affected by the length of each span and characteristic parameters of downburst to some extent.
- Due to the adopted low turbulence intensity and the introduction of conductor's motion state in the load calculation, the effect of the fluctuation component on the response is fairly small. Moreover, in a moving downburst, longer risk duration of flashover is found, which may lead to a higher possibility of the forced outage.
- Due to the uncertainty of the initial location, motion path, occurrence and duration time of the moving downburst, it should only be considered in some particular areas. For a particular SIS's precaution of downburst-induced flashover, a recommended calculation case, that the storm center moves directly through the given SIS in the direction perpendicular to the transmission line, is given, whose results may reflect the results of all the cases in an acceptable range.

Acknowledgements

The research is financial supported by the National Science Foundation of China (51378468) & Science and Technology Project of State Grid Corporation of China, and Science and Technology Project of State Grid Zhejiang Electric Power Company (Grant No. ZDK 013-2012, kxk 2012-017).

References

- Aboshosha, H. and EI Damatty A. (2013), "Downburst induced forces on the conductors of electric transmission lines and the corresponding vulnerability of towers failure", *Proceedings of the CSCE 2013 General Conference*, Montreal, Quebec, May 29-June 1.
- Achenbach, E. and Heinecke, E. (1981), "On vortex shedding from smooth and rough cylinders in the range of Reynolds numbers 6×10^3 to 5×10^6 ", *J. Fluid Mech.*, **109**, 239-251.
- Chay, M.T. and Letchford, C.W. (2002), "Pressure distributions on a cube in a simulated thunderstorm downburst—Part A: stationary downburst observations", *J. Wind Eng. Ind. Aerod.*, **90**, 711-732.
- Chen, L. and Letchford, C.W. (2004), "A deterministic-stochastic hybrid model of downbursts and its impact on a cantilevered structure", *Eng. Struct.*, **26**, 619-629.
- Chen, L. and Letchford, C.W. (2005), "Simulation of extreme winds from thunderstorm downbursts", *Proceedings of the Tenth Americas Conference on Wind Engineering*, Baton Rouge, Louisiana, USA, May 31-June 4.
- Dempsey, D. and White, H. (1996), "Winds wreak havoc on lines", *Transmission and Distribution World*, **48**(6), 32-37.
- EI Damatty, A. and Aboshosha, H. (2012), "Capacity of Electrical Transmission towers under downburst loading", *Proceedings of the 1st Australasia and South-East Asia Structural Engineering and Construction Conference*, Perth, Australia, Nov 28-Dec 2.
- Fujita, T.T. (1985), "Manual of downburst identification for project NIMROD", *SMRP Research Paper 156*, University of Chicago, 104.
- Hawes, H. and Dempsey, D. (1993), "Review of recent Australian transmission line failures due to high intensity winds", *Paper presented at Work-shop on High Intensity Winds on Transmission Lines*, Buenos Aires, Argentina, 19-23.
- Hu, Y. (2004), "Study on trip caused by windage yaw of 500kV transmission line", *High Voltage Engine.*, **30**(8), 9-10.
- Jia, B.Y., Geng, J.H., Fang, C.H. *et al.* (2012), "Influence of wind speed and direction on flashover characteristic of composite insulators", *High Voltage Engine.*, **38**(1), 75-81.
- Kanak, J., Benko, M., Simon, A. *et al.* (2007), "Case study of the 9 May 2003 windstorm in southwestern Slovakia", *Atmos. Res.*, **83**, 162-175.
- Li, C., Li, Q.S., Xiao, Q. *et al.* (2012), "A revised empirical model and CFD simulations for 3D axisymmetric steady-state flows of downbursts and impinging jets", *J. Wind Eng. Ind. Aerod.*, **102**, 48-60.
- Li, C.Q. (2000), "A stochastic model of severe thunderstorms for transmission line design", *Probabilist. Eng. Mech.*, **15**, 359-364.
- Lin, W.E., Savory, E., McIntyre, R.P. *et al.* (2012), "The response of an overhead electrical power transmission line to two types of wind forcing", *J. Wind Eng. Ind. Aerod.*, **100**, 58-69.
- Liu, X.H., Yan, B., Lin, X.S. *et al.* (2009), "Numerical simulation of windage yaw of 500kV UHV Transmission lines", *Eng. Mech.*, **26**(1), 244- 249.
- Long, L.H., Hu, Y., Li, J.L. *et al.* (2006), "Study on windage yaw discharge of transmission line", *High Voltage Engine.*, **32**(4), 19-21.
- Lu, M. (2014), *Typical failure analysis of transmission line*, China Electric power press, Beijing, China.
- Mara, T.G. and Hong, H.P. (2013), "Effect of wind direction on the response and capacity surface of a transmission tower", *Eng. Struct.*, **57**, 493-501.
- McCarthy, P. and Melsness, M. (1996), "Severe weather elements associated with September 5, 1996 hydro tower failures near Grosse Isle, Manitoba, Canada", *Manitoba Environmental Service Centre*, Environment Canada, 21pp.
- Oliver, S.E., Moriarty, W.W. and Holmes, J.D. (2000), "A risk model for design of transmission line systems against thunderstorm downburst winds", *Eng. Struct.*, **22**, 1173-1179.
- Pan, F., Sun, B.N., Lou, W.J. *et al.* (2008). "Random wind-induced dynamic response of long-span roof to thunderstorm downbursts in the time domain", *Acta. Aerodyn. Sin.*, **26**(1), 119-125.

- Raghavan, K. and Bernitsas, M.M. (2011), "Experimental investigation of Reynolds number effect on vortex induced vibration of rigid circular cylinder on elastic supports", *Ocean Eng.*, **38**(5-6), 719-731.
- Savory, E., Parke, G.A.R., Zeinoddini, M. *et al.* (2001), "Modelling of tornado and microburst-induced wind loading and failure of a lattice transmission tower", *Eng. Struct.*, **23**(4), 365-375.
- Shahata, A.Y., EI Damatty, A. and Savory, E. (2005), "Finite element modeling of transmission line under downburst wind loading", *Finite Elem. Anal. Des.*, **42**(1), 71-89.
- Shahata, A.Y. and EI Damatty, A. (2007), "Behaviour of guyed transmission line structures under downburst wind loading", *Wind Struct.*, **10**(3), 249-268.
- Shahata, A.Y. and EI Damatty, A. (2008), "Failure analysis of a transmission tower during a microburst", *Wind Struct.*, **11**(3), 193-208.
- Shahata, A.Y., Nassef, A.O. and EI Damatty, A. (2008), "A coupled finite element-optimization technique to determine critical microburst parameters for transmission towers", *Finite Elem. Anal. Des.*, **45**, 1-12.
- Sun, C.B. (2003), *Power Transmission Line*, China Electric Power Press, Beijing, China.
- Sun, Z.M. (2010), *Analysis of Transmission Line Galloping and Research on Anti-galloping Technology*. College of Civil Engineering and Architecture, Zhejiang university, Hangzhou, China.
- Wang, S.X., Wu, G.N., Fan, J.B. *et al.* (2008), "Study on flashover of suspension insulator string caused by windage yaw in 500kV transmission lines", *Power Syst. Technol.*, **32**(9), 65-69.
- Yan, B., Lin, X.S., Luo, W. *et al.* (2010), "Research on dynamic wind load factors for windage yaw angle of suspension insulator strings", *Eng. Mech.*, **27**(1), 221-226.

